6 Model Description

This chapter describes modeling for tidal hydrodynamics, macrophyte interactions with hydrodynamics, and fine-sediment resuspension and transport. Laguna Madre, typical of ecosystems with submersed aquatic vegetation, is relatively shallow, physically stable, and of moderate hydrodynamic energy. Wind waves are critical to sediment resuspension. Feedbacks exist, both forward and backward, between bed shear-stress, erosion, and submersed aquatic vegetation as described in Chapter 1. Therefore, special model features that could describe these components and feedbacks were developed and implemented in the U.S. Army Corps' TABS-MDS in this study. Shear stress interactions are shown schematically in Figure 1.

General Model Features

TABS-MDS is an enhanced version of the finite-element RMA10-WES and RMA10 models (King 1993). Geometric flexibility, high-dimensional representation, and computational efficiency are desirable attributes of a numerical hydrodynamic model. The finite element approach offers the greatest geometric flexibility. The TABS-MDS model uses finite elements and a Galerkin variant of the weighted residual solution method. It has the capability for 3-D, depth- and laterally-averaged 2-D , and 1-D modes and adapts to wet and dry areas as water level changes. The spatial domain modeled has irregular bathymetric and boundary features which are most accurately represented by irregular, unstructured grids or meshes.

Two-dimensional depth-averaged model meshes were developed for Laguna Madre with use of the U.S. Army Corps' Surface water Modeling System (SMS©). Detailed shore-to-shore bathymetric data from 1995 were compiled and used to develop a model mesh of about 20,000 nodes. The mesh has highest resolution near the navigation channel and certain dredged material placement areas.

Settling and deposition process descriptors were developed for a multiple grain-size class numerical sediment transport model implemented in TABS-MDS. Coupling of numerical grain classes was based on a previous analytic description of grain-spectra change during settling. A layered-bed algorithm was developed for TABS-MDS with variable silt concentrations by layers. Layers depend on initial conditions and on erosion and deposition histories. Erodibility is also linked to the structure of the bed. The effect of suspended sediment concentration

on floc settling rate due to flocculation was included in the model. Descriptions of these features are given later in this chapter.

Other TABS-MDS model features were developed to account for (a) spatially-varying atmospheric friction coefficients to improve computation in very shallow and vegetated areas; (b) partitioning of atmospheric shear stress to account for shear stress going to waves and currents; and (c) bed-sheltering effects of seagrass. The shear-stress sheltering factors for seagrasses are described later in this section. Atmospheric shear stress and its partitioning are described in Chapter 2.

Bed material types

TABS-MDS uses a system of indices to distinguish and define local sediment and frictional characteristics of the bed. Bed layer thickness and density structure, grain-size distribution, SAV bed-sheltering factors, friction factors, SAV canopy heights were specified by bed material types. Data on bed material grain size and seagrass species were dominant in the classification of bed material type. Model roughness coefficient assignments were based on the sediment type, bed roughness features, and the species of submersed aquatic vegetation by elemental material types according to the unions of these parameters.

Bed sheltering by submersed vegetation

Submersed macrophyte vegetation reduces the ability of a flow to resuspend material from the bed (Lopez and Garcia 1998), decreases suspended sediment transport capacity, and reduces momentum transfer to the bed-sediment surface. It absorbs momentum and transfers it to the bed directly through its stems. By doing so, plants have been reported to change bed particle-size distribution, organic content, and bed morphology. Likewise, changes in the configuration of seagrass beds can appreciably change large-scale bed and near-shore morphology (Fonseca 1996).

Fonseca and Fisher (1986) estimated a Shields' sediment-entrainment function under seagrass canopies (Fs') based on the initiation of sediment movement. A normal-valued Shields entrainment function Fs for a bare bed with the sediment particle size used in these experiments would be expected to be about 0.06 while Fonseca and Fisher (1986) found much higher values. This finding indicated that greater total shear stress was required to initiate sediment movement under seagrasses, and much of the total shear stress was not acting on the bed. The increased Fs' compared to Fs can be interpreted as a decrease in the bed shear stress for the same total shear stress. Then the ratio Fs / Fs' expresses the fraction of the total shear stress reaching the bed. Results for the four seagrass species from the data of Fonseca and Fisher (1986) are presented in Table 34. The fraction of shear stress reaching the bed appears, in general, to be inversely related to the frictional effect expected from the seagrass species.

Table 34	
Estimated Bed Sheltering Factors for Seagrass Species	
Species	*Fs / Fs'*
H.w.	0.21
S.f.	0.66
T.t.	0.12
Z.m.	0.21

Lopez and Garcia (1998) performed numerical simulations which indicated that the fraction of the total shear stress reaching the bed might be a function of plant density. As indicated in the last subsection, the experimental data of Gambi et al. (1990) indicated that over a density range of 400 to 1,200 shoot/m^2, friction factors were about constant. While Gambi et al. (1990) did not measure bed shear stress, they found under-canopy flow to be affected by shoot density. This finding might indicate that the sheltering effect is seagrass-density dependent. More detailed laboratory and field measurements are needed to improve the description of sediment resuspension within submersed vegetation (Lopez and Garcia 1998).

Model limitations

Because of limits in our ability to perform massive computations, compromises are made to insure that a given model can be operated in an economical manner for the problem for which it was developed. For any specific model domain and ecosystem, other tradeoffs are required in the model spatial resolution, state variables, temporal resolution, and simulation duration.

Relatively small man-made structures, including channels, depth features, flow features such as gyres, and/or recirculations, require appropriate spatial resolution to be resolved in model grids and to be accurately computed. An adequate horizontal mixing formulation, such as that of Smagorinsky (1963) described later, may be required. It should be noted that accurate, spatially-resolved bathymetric data are important in general. "Geometry is everything" is a good rule of thumb for hydrodynamic modeling.

Langmuir circulation cells, often observed in Laguna Madre, are ubiquitous in shallow aquatic systems and consist of wind-aligned roll vortices which trap floatable materials in windrows. These long, spiraling circulations have alternating rotations. Plant litter often marks the downwelling convergences between cells. In shallow water, these circulations reach the bottom and respond rapidly to wind changes. Downwelling current speeds can be of the same order (cm/sec) as the mean flows (Leibovich 1983) and could dominate over- to under-canopy mass exchanges. Langmuir circulations are produced by interactions between wave orbital motions and the background shear-flow (Faller 1969). Dispersion within Langmuir cells is many times higher than the background turbulent values (Faller and Auer 1988). Cross-cell dimensions are only about

three times the water depth, so circulation cells are too small to be resolved in hydrodynamic models (and would require special model formulations).

Hydrodynamic Model

The bases for governing flow equations are the 3-D Navier-Stokes equations. With Boussinesq and hydrostatic assumptions, and with an eddy-viscosity closure on the Reynolds stress terms, the 3-D Navier-Stokes equations are expressed for TABS-MDS in two momentum equations and an integrated continuity equation as follows:

$$\rho \, \frac{Du}{Dt} \, - \, \nabla \cdot \sigma_x \, + \, \frac{\partial P}{\partial x} \, - \, \Gamma_x \, = \, 0 \tag{46}$$

$$\rho \, \frac{Dv}{Dt} \, - \, \nabla \cdot \sigma_y \, + \, \frac{\partial P}{\partial y} \, - \, \Gamma_y \, = \, 0 \tag{47}$$

$$\frac{\partial h}{\partial t} \, + \, u_\zeta \, \frac{\partial \zeta}{\partial x} \, - \, u_a \, \frac{\partial a}{\partial x} \, + \, v_\zeta \, \frac{\partial \zeta}{\partial y} \, - \, v_a \, \frac{\partial a}{\partial y} \, + \, \int_a^\zeta \left(\frac{\partial u}{\partial x} \, + \, \frac{\partial v}{\partial y} \right) dz \, = \, 0 \tag{48}$$

where

$$\sigma_x \; = \; \begin{pmatrix} E_{xx} \, \dfrac{\partial u}{\partial x} \\[6pt] E_{xy} \, \dfrac{\partial u}{\partial y} \\[6pt] E_{xz} \, \dfrac{\partial u}{\partial z} \end{pmatrix} \; ; \quad \sigma_y \; = \; \begin{pmatrix} E_{yx} \, \dfrac{\partial v}{\partial x} \\[6pt] E_{yy} \, \dfrac{\partial v}{\partial y} \\[6pt] E_{yz} \, \dfrac{\partial v}{\partial z} \end{pmatrix} \tag{49}$$

$D/Dt = \partial/\partial t + u \, (\partial/\partial x) + v \, (\partial/\partial y) + w \, (\partial/\partial z)$, $u,v,w = x,y,z$ velocity components, t is time, P is pressure, ρ is density, ∇ is the gradient operator, h is the depth, u_ζ, $v_\zeta = x,y$ velocity components at the water surface, ζ is the water surface elevation, u_a, $v_a = x,y$ velocity just above the bed, and a is the bed elevation. Γ_x, $\Gamma_y = x,y$ combined Coriolis, bed-friction, and wind forces:

$$\Gamma_x \; = \; \rho \Omega v \; - \; \frac{\rho g u_a (u_a^2 + v_a^2)^{1/2}}{C^2} \; + \; \psi U_a^2 \cos(\Theta)$$

$$\Gamma_y \; = \; -\rho \Omega u \; - \; \frac{\rho g v_a (u_a^2 + v_a^2)^{1/2}}{C^2} \; + \; \psi U_a^2 \sin(\Theta)$$

$\Omega = 2\omega \sin(\phi)$, ω is the rate of angular rotation of the earth, ϕ is the local latitude, g is the gravitational acceleration, C is a Chezy or Manning friction formulation, ψ is a coefficient from Wu (1980), U_a is the standard-height wind speed, and θ is the wind direction counterclockwise from easterly. The atmospheric drag expression developed in Chapter 2 was implemented to optionally replace that of Wu. The Manning's friction formulation is applied over three ranges of relative roughness height as described in Appendix A.

TABS-MDS uses the continuity equation

$$\frac{\partial u}{\partial x} + \frac{\partial v}{\partial y} + \frac{\partial w}{\partial z} = 0 \tag{50}$$

to solve for w. In TABS-MDS, the continuity equation is solved in the differentiated form

$$\frac{\partial^2 w}{\partial z^2} = -\frac{\partial}{\partial z}\left(\frac{\partial u}{\partial x} + \frac{\partial v}{\partial y}\right) \tag{51}$$

after applying appropriate boundary conditions to the surface and bottom.

In TABS-MDS, the z coordinate is transformed to allow computational nodes to be located at the time-varying water and bed surfaces and variable vertical node spacing. The transformed vertical coordinate is

$$z^{\nabla} = \frac{(z - a)}{(b - a)}h + z_b \tag{52}$$

where b is the fixed vertical location of the water surface, h is the time-varying water surface, a is the elevation of the fixed bed, and z_b is the time-varying location of the bed. For example:

$$\frac{\partial P}{\partial x} = \frac{\partial P}{\partial x^{\nabla}} + \frac{\partial P}{\partial z^{\nabla}}\frac{\partial z^{\nabla}}{\partial x^{\nabla}} \tag{53}$$

where $x^{\nabla}, y^{\nabla} = x, y$ are the transformed horizontal coordinates. In this transformation $z^{\nabla} \approx z$ so that the transformed vertical coordinate surfaces are nearly horizontal.

A horizontal turbulence-closure scheme (Smagorinsky 1963; see review by Speziale 1998) is used to dynamically set eddy viscosity terms in Equation 4 and horizontal diffusion coefficients in transport equations to be described later. The Smagorinsky method of describing horizontal eddy-viscosity and diffusivity coefficients uses mesh-element velocity gradients and areas in a generalization of a mixing-length representation for these terms.

Models in 1-D and 2-D are formulated by integrating the 3-D equations of motion over appropriate dimension(s) as described in Appendix A. In doing so, 1-D and 2-D models lose the capability to predict variations in the missing dimension(s) and some assumptions must be introduced. However, the 2-D depth-averaged approach is justified and well suited for shallow, near-homogeneous systems such as Laguna Madre.

Frictional effects of submersed vegetation

Friction coefficients must be specified in hydrodynamic models. However, our knowledge of frictional effects related to submersed plants is insufficient and incomplete to accurately calculate flows and shear stresses. Bed shear stress is

critical to sediment resuspension modeling, and as mentioned earlier, submersed vegetation shelters the bed from shear stress generated largely by vegetation-induced drag.

Current friction. Hydrodynamic friction for seagrass areas is complicated by the fact that it can not be characterized by a single coefficient. The magnitude of the frictional effect depends on the mechanical properties of the plants, how they bend in the current, and the area and distributions of their leaves. Canopy height is a key factor, and since it is dynamic with respect to the flow, the friction coefficient changes with even small changes in flow speed. As the vegetation bends, the boundary roughness is much reduced.

The Darcy friction factor f decreases with increased flow until plants are fully deflected. A plot of data presented by Gambi et al. (1990), demonstrating the decrease in f with increasing u and the lack of a consistent shoot-density effects, is shown in Figure 65. For those data, canopy height $y_c = 0.145$ m, water depth $h = 0.235$ m, and the friction parameter values were developed. Analyses indicated that at flows less than a few centimeters per second the canopy height was unchanged and frictional characteristics were constant.

Madsen et al. (2001) report on observed Manning's n values for rivers with submersed plant beds. Depending on plant biomass, values of 0.03 to 0.3 were found, for small rivers, to be inversely related to river discharge. In a densely vegetated stream, n was also sensitive to discharge and was reduced from 0.2 to 0.1 when macrophytes were harvested.

Wave friction. Data on the wave-frictional characteristics of seagrasses are very sparse. Fonseca and Cahalan (1992) performed laboratory wave-damping tests on several seagrass species collected from the Laguna Madre. The wave Reynolds numbers for these experiments were low (220 to 850), making the bare-bed resistance hard to estimate.

Wave friction-roughness heights k_n were inferred from wind and wave data from the Laguna Madre (see Chapter 2) instead of from bed-grain size. For bare areas, k_n values were near the expected value of about 0.001 m. For *T.t.* vegetated areas, k_n values were about 0.2 m.

Sediment Transport Model

Three components needed to successfully apply a sediment model to a real-world situation are (a) suspended- and bed-sediment data adequate to the purpose; (b) a correct model formulation; and (c) accurate shear stresses from a hydrodynamic and/or wave model. Shallow, vegetated aquatic systems like Laguna Madre have low TSM and currents, and the sediment material in suspension is fine-grained under most conditions. SAV respond to frequently occurring underwater light conditions and can tolerate short periods of low-light. Therefore, since the interest here is in the normal range of TSM conditions and not extreme events, fine-grained silts and clays are the subject of the modeling described in this section.
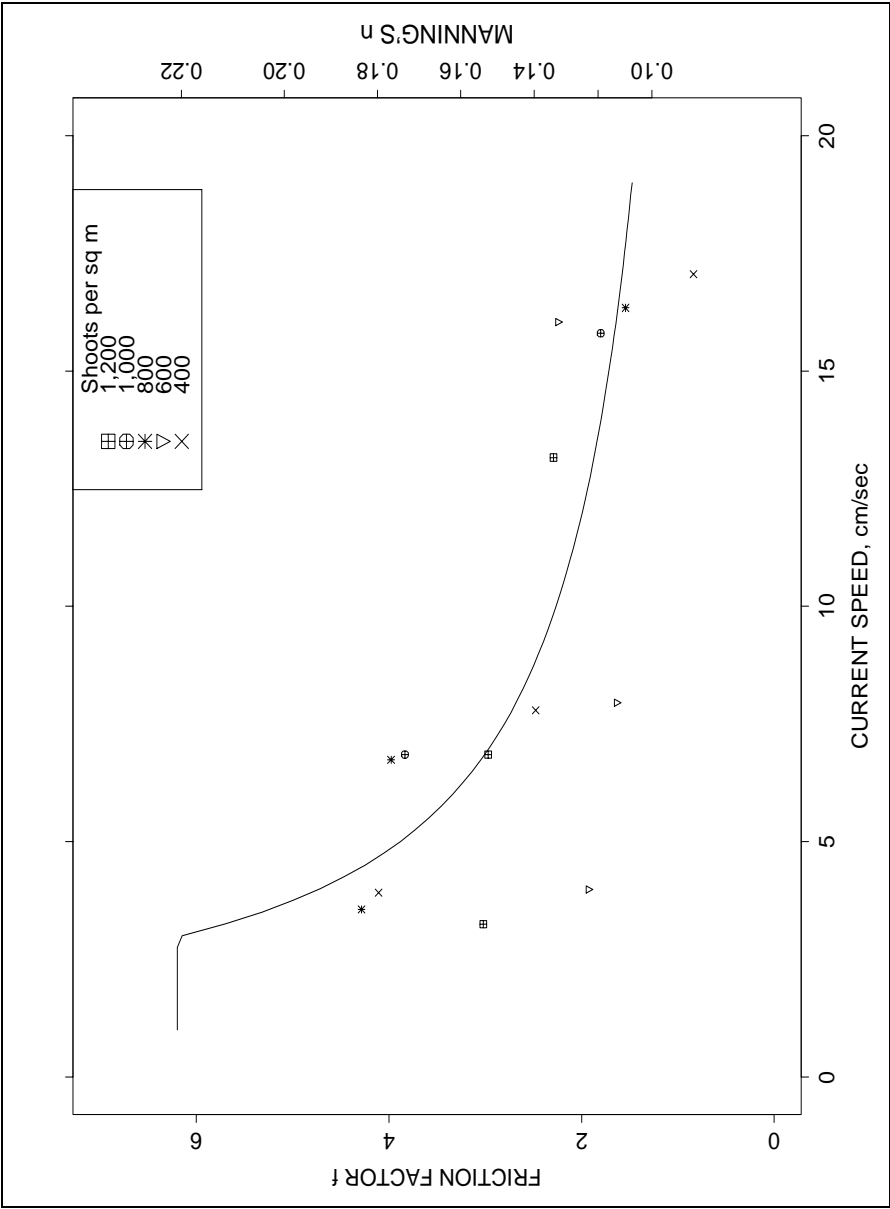
Figure 65. The relation of friction factors f (left) and Manning's n (right) to current speed u for the data of Gambi et al. (1990)

For three dimensions, the advection-diffusion equation for sediment transport is

$$\frac{Dc}{Dt} - \frac{\partial}{\partial x}\left(D_x \frac{\partial c}{\partial x}\right) - \frac{\partial}{\partial y}\left(D_y \frac{\partial c}{\partial y}\right) - \frac{\partial}{\partial z}\left(D_z \frac{\partial c}{\partial z}\right) = 0 \tag{54}$$

where c is the concentration of suspended material, Dc/Dt is the total derivative that includes advection, and D_x, D_y, D_z = x, y, z eddy diffusivity components for sediment mass. Diffusivities generally include the effects of small-scale motions such as Langmuir circulations, as well as turbulence. The effective vertical velocity w_e is substituted for w in the total derivative Dc/Dt where $w_e = w - W_s$, and W_s is the settling velocity. The surface boundary is given a no-flux condition and the bottom boundary condition is

$$\frac{\partial}{\partial z}\left(w_e c - D_z \frac{\partial c}{\partial z}\right) = E - D \tag{55}$$

where E is the vertical erosional flux and D is the vertical depositional flux. Dimensions of the erosion and deposition fluxes are mass per unit area per unit time. The sediment model formulations described later in this section specify expressions for E and D and conditions over which they operate.

Cohesive sediment characteristics

Important differences between coarse- and fine-grained sediment transport characteristics can be attributed to cohesive effects. Cohesive forces act at very small distances and are affected by clay mineralogy, ion content and composition, pH, and temperature. Cohesive bonding under field conditions also includes organic coatings and steric bonds of organic origin. Cohesion acts to form several structural levels of progressively weaker aggregation for clay minerals. Three general differences between cohesive and coarse-grained (greater than 62 µm) sediment transport under moderate shear stresses included in the sediment model include:

1. Cohesive sediments are only transported in suspended state.
   Coarse-grained sediments are also transported in quasi-contact with the bed as bed load.
2. Cohesive sediments are not transported as dispersed, individual particles.
   Flocculation increases settling velocities by many orders of magnitude and is responsible for deposition.
3. Cohesive sediment beds undergo appreciable volume and erodibility changes with time.
   When rapid deposition occurs, deposits are light and have little hydraulic shear strength. Cohesive beds can be uniform but more often are vertically stratified by density and hydraulic shear strength.

Since cohesion varies with mineralogy and other factors as described earlier, site-specific information was used to characterize grain-class transport properties for Laguna Madre.

Grain-class formulation

Multiple-grain class fine-grained sediment model formulations have been presented by Lavelle (1993), Le Hir et al. (1993), Chester and Ockenden (1997), and Teeter (2001a and b). By admitting multiple grain classes, this formulation included a higher degree of realism than that found in a single-grain class formulation for the case of a system with relatively wide-ranging particle sizes such as Laguna Madre.

Sediment grains strongly affect the flocculation process (Kranck and Milligan 1992), along with a host of other conditions, such as temperature, salinity, ionic content, pH, clay mineralogy, and organic constituents. Sediment grains are better model state variables than flocs since they are conservative constituents in both suspension and bed, affect both erosion and deposition, and are more easily measured in the environment. Grain classes are coupled by cohesion, and this coupling must be accounted for in multiple-grain class models.

Because fine-grained cohesive transport processes are not dependent on individual particle size intrinsically, grain-class size designations are nominal in that they do not govern transport properties directly. In the model, the finest class represents the most cohesive clay and fine-silt sized particles and is referred to as the cohesive fraction. Evidence suggests that this class behaves as a unit and dominates several transport processes and the character of the sediments as a whole (Teeter and Pankow 1989b; Stevens 1991a and b). Silts are divided into a variable number of classes, though evidence suggests that they act as a continuous distribution.

Size-spectra response to deposition

Coupling of grain classes during erosion and deposition is apparent in grain-size measurements taken under these conditions. The grain-coupling scheme used in this model assumes that fine-grained, cohesive sediments are deposited along with silts even though shear stresses are too high for them to deposit on their own. Serial coupling between grain-size classes is used to promote log-normal trends in the resulting size distributions, as discussed later in this section.

Floc and grain-size particle diameter (D) spectra can be parameterized in terms of three variables Q, m, and K (Kranck 1980; Kranck and Milligan 1992). Q, which depends on the total particle concentration and the shape of the distribution, is defined by a concentration $C_o(D)$ at 1 μm diameter. The variable m defines the slope of the fine end (small-size) of the distribution when plotted log-log. The variable K is related to the fall off at the coarse end of the distribution. Kranck and Milligan (1992) found m to be constant for both floc and grain distributions. Substituting for $W_s t/H$, the equation describing the distributions is

$$C(D) = QD^m \exp(-KAD^2) \tag{56}$$

where AD^2 defines a Stokes' settling rate, $A = g(\rho_f - \rho_l)/18\nu\rho_l$, g is the acceleration of gravity, ν is the kinematic viscosity of the fluid, ρ_f is the floc

density, and ρ_l is the fluid density. Their distribution model Equation 56 was fit to observed spectra taken during both decreasing and increasing suspension concentrations. It reflects how changing suspension concentrations affect grain spectra. Grain and floc spectra covering the range of distribution parameters found by Kranck and Milligan (1992) for San Francisco Bay suspended sediments are shown in Figure 66. A Laguna Madre sediment was found to follow this grain-distribution pattern during settling, as shown in Figure 43. Settling velocities by size class were also determined using sediments from New Bedford Harbor estuary by Teeter (1993).

The values of the Q_g, K_g, and K_f distribution parameters changed with total suspension concentrations while m values remained about constant. Coupling between grain classes caused fine sediment to deposit when a well-sorted sediment of the same size would have remained in suspension. Links between floc and grain settling were also demonstrated by Kranck and Milligan (1992), as both maximum grain and floc size varied with total concentration and with bottom shear stress. Though the development of their distribution model Equation 56 was based on particle removal by settling, spectra observed during resuspension followed the same patterns in reverse.

The distribution model Equation 56 is most useful in describing measured size spectra and explaining the effects of various settling modes on spectral shapes. Numerical algorithms which produce results similar to observed- and model-grain spectra were developed. They will be presented later in this section. Grain class settling rates are calculated to span floc settling rate distributions. Depositional fluxes are coupled from the coarsest to the finest grain-size class in proportion to class concentrations, consistent with the analytic model of Kranck and Milligan (1992) and other previously observed grain-size distributions.

Concentration effects on settling velocity

Floc settling velocity is defined as the sinking rate in quiescent fluid. It affects vertical transport and distribution in the water column and maximum rate of deposition. Settling velocity of cohesive sediments varies with concentration and with fluid shear rate (Camp 1946; Krone 1962; Van Leussen 1989; and Kranck and Milligan 1992). Suspension concentration affects cohesive sediment aggregate collision frequency, floc size, and settling rate. Enhanced settling occurs over a concentration range from a lower concentration limit C_{ll} to an upper concentration limit C_{ul}. Below C_{ll}, particle collisions are too infrequent to promote aggregation. Concentration limits for enhanced settling are shown schematically in Figure 67. C_{ll} is typically 50 to 300 mg/l depending on sediment characteristics. Laboratory settling tests indicated that C_{ll} is 50 mg/l or less for Laguna Madre channel sediments (see Figure 40). At C_{ul}, collisions are so numerous that particles interact completely, causing all floc settling rates to converge to one value. At concentrations greater than C_{ul}, particle interactions begin to hinder settling, and dense suspensions settle as masses. Camp (1946) found the onset of concentration-hindered settling to be 1 to 5 kg/m^3 for turbid river water. The first author has found C_{ul} to be 1 to 10 kg/m^3 for estuarine sediments. Observed settling characteristics of Laguna Madre sediments indicate
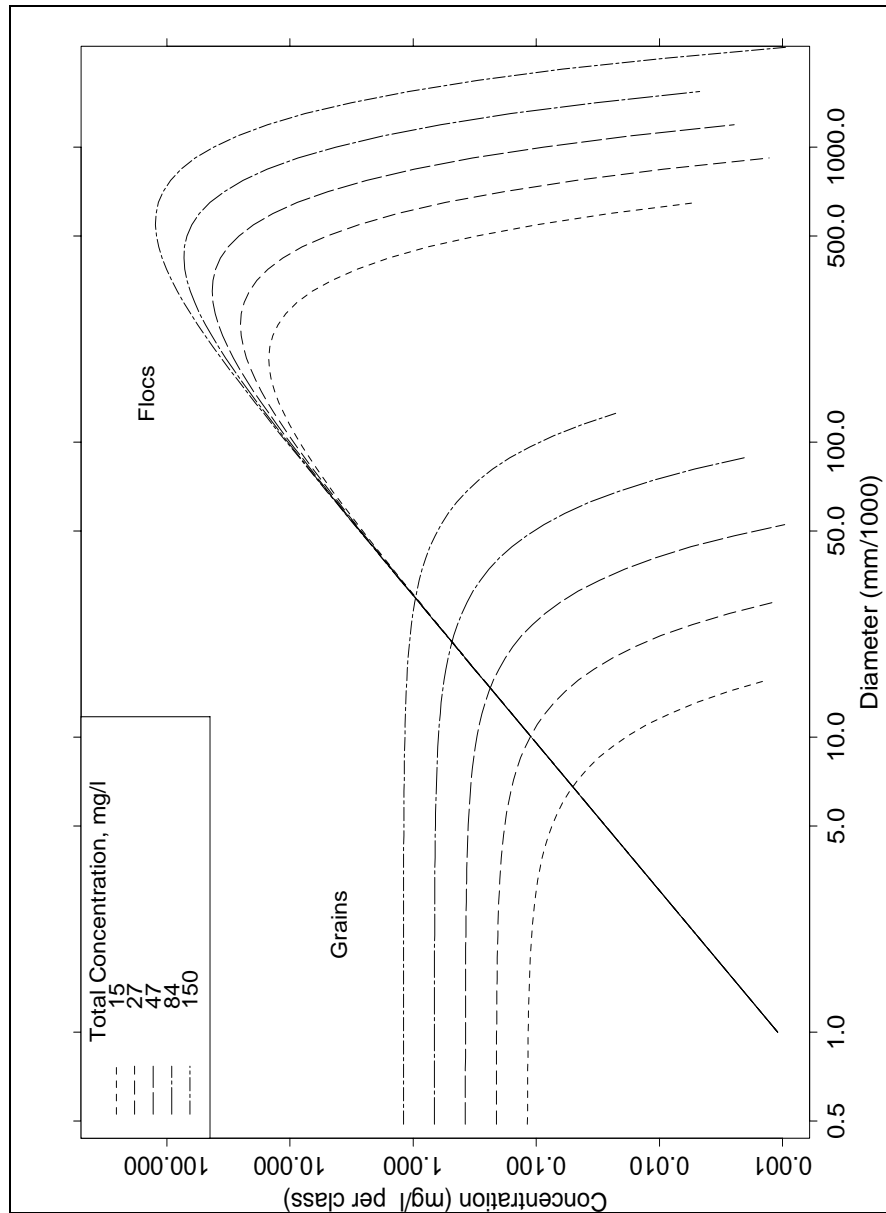
Figure 66. Floc (right) and grain (left) spectra based on tidal measurements of Kranck and Milligan (1992) for varying suspended sediment concentrations
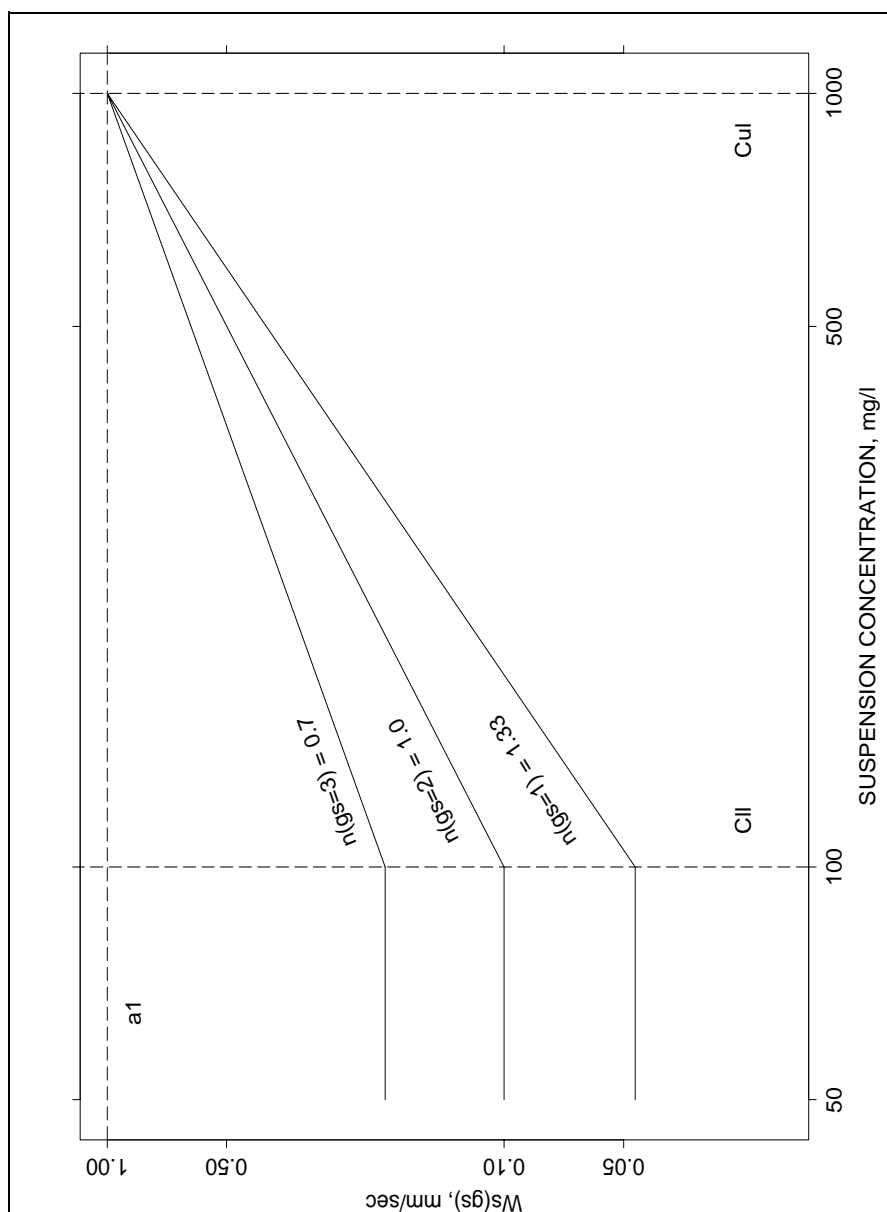
Figure 67. Definition of upper and lower limiting concentrations for enhanced settling, and example grain class exponents

the maximum settling rate occurs at about 3 kg/m^3, as reported in Chapters 4 and 5.

For the multiple-grain size model, the general form for grain-class settling velocity $W_s(gs)$ is

$$W_s(gs) = a_1 \left(\frac{C}{C_{ul}} \right)^{n(gs)}, \quad C_{ll} \leq C \leq C_{ul} \tag{57}$$

where a_1 is a grain-size, class-average maximum floc settling velocity, C is the total concentration for all grain size classes, gs is the grain-class index ranging from 1 to the number of grain-size classes, $n(gs)$ is an exponent, and C_{ll} and C_{ul} are mass-weighted average lower and upper reference concentrations, respectively, over which concentration-enhanced settling occurs. The mass-weighted averages are taken over grain size classes. For example,

$$a_1 = \frac{1}{C} \sum_{gs=1}^{NS} a_1(gs) \, C(gs) \tag{58}$$

where NS is the number of grain classes. The normalized concentration C/C_{ul} is used in Equation 57 so that the dimensions of $a_1(gs)$ and a_1 are mutually consistent with W_s, and not affected by the magnitude of $n(gs)$. At $C \geq C_{ul}$, $W_s(gs)$ equals a_1 for all gs classes. At $C \leq C_{ll}$, settling rates are independent of concentration and are equal to $W_s(gs)$ evaluated at C_{ll}.

The range of $n(gs)$ defines the span of the floc settling distribution as in the hypothetical case shown in Figure 67. Though the smallest grains are not always associated with the smallest flocs and the largest grains with the largest flocs, the effect of Equation 57 is to produce distributions of $W_s(gs)$ that reflect the effect of grain composition on floc settling spectra. Additional coupling between grain-size classes is imposed during deposition, as described later, such that deposition of a given grain-size class is not necessarily related to its settling velocity.

Settling experiments performed concurrently with particle-size analyses, as reported in Chapter 4, were used to estimate settling velocities for specific size classes. The exponents $n(gs)$ for Laguna Madre were determined empirically by use of information from settling tests conducted over a range of concentrations. See Figure 42. After appropriate percentiles to represent the grain-size classes were selecting, fits to settling data were made. The exponent n has been determined to range below a value of about 1.33 as estimated with this method. Teeter and Pankow (1989a) found that n's for the 50 and 75 percentile values were progressively less than for the 25 percent slowest settling fraction.

Deposition rate

Deposition removes sediment from the water column at a rate equal to the product of effective settling and concentration. To deposit, sediment must transit the zone just above the bed, which can have very high shear rates. Previous laboratory experiments (Krone 1962; Teeter and Pankow 1989b) have observed that effective W_s based on deposition are lower than those measured in the water column. The calculation procedures presented in this section first assess the

deposition process for individual grain classes, then couple grain-size classes such that the final result depends on deposition of the coarsest active class and the grain-size spectra.

Potential deposition of each grain-size class is first assessed. Deposition is assessed differently for the cohesive fraction than for silts. The cohesive fraction is taken to follow Krone's deposition law (Krone 1962), which uses the concept of a critical shear stress for deposition and the depositional probability. The effective settling velocity is the settling velocity times the depositional probability P defined by Krone (1962) and for the finest cohesive fraction is

$$P = \left(1 - \frac{\tau}{\tau_{cd}} \right) , \quad \tau < \tau_{cd} \tag{59}$$

where τ is the bed shear stress and τ_{cd} is the critical threshold shear stress for deposition. According to Equation 59, all sediment eventually deposits at shear stresses less than the critical value.

For each silt class, upper and lower shear-stress threshold values are defined slightly differently from the way those used for the cohesive fraction are. The lower or critical depositional shear stress is defined as that value below which all material is free to deposit. Below this threshold, silt deposition depends only on concentration and settling velocity ($P = 1.0$). At shear stresses between the upper and lower critical values, silt sediment fractions erode or deposit at rates linearly related to the bed and threshold shear stresses.

The upper or critical erosional shear stress is defined as that value above which all material of this class will remain in suspension ($P = 0$), but it is not linked explicitly to erosion. Erosion of a silt fraction is first dependent on the erodibility of the cohesive fraction. That is, silt is held in a cohesive matrix and is not free to erode unless the bed shear-stress exceeds the erosional threshold for the cohesive fraction, as described in Chapter 4. Shear-stress ranges are specified to be contiguous for contiguous grain classes. That is, the upper shear-stress threshold τ_{ce} for one class is the same value as the lower threshold τ_{cd} for the next coarser class.

After the potential deposition from each grain class has been assessed, grain classes are coupled such that spectral shapes follow the distribution model of Equation 56. As noted earlier, coupling between grain classes causes some sediment to deposit when a well-sorted sediment would remain in suspension. For the deposition of grain classes to be proportional as in Equation 56, settling velocities over those grain classes that are depositing must be equal. Other controls are also introduced to ensure that the algorithm is capable of forming steady-state suspensions at a given bed shear-stress level. Thus, if F is the depositional flux, gs is a grain class with $P \approx 0$, and $gs+1$ is a larger-sized depositional grain class

$$F(gs) = \frac{d_1\, C(gs)\, F(gs+1)}{(C(gs+1) + d_2)} , \qquad P(gs) < 0.05 \tag{60}$$

where d_1 controls the exact proportion between the fluxes, and d_2 limits flux of smaller grains as $C(gs+1)$ tends toward zero. The deposition algorithm introduces two parameters to control the proportional deposition. Data indicate that $d_1 \approx 1$ or slightly below.

Threshold shear-stresses for mutually exclusive erosion and deposition are used in the model formulation to be consistent with previous laboratory investigations. Model deposition and erosion laws treat silt and clay fractions differently, yet couple them during certain modes of vertical transport. Models with up to seven grain classes are compared to laboratory flume tests which formed steady state suspension concentrations during deposition.

While a well-sorted cohesive suspension will steadily deposit in a flow below a critical shear stress (Krone 1962), a suspension of silts and clays will partially deposit to a steady state, constant-suspension concentration level (Partheniades et al. 1968). A similar paradox is that clay minerals segregate during transport in a manner that is similar to their settling rates based on dispersed particle size (Gibbs 1977). Thus, even though grain classes are coupled by cohesion, dispersed particle size affects transport properties, and size-distribution imprints form clearly detectable patterns in estuarine and lake sediments.

Erosion rate

The erosion flux depends first on the erosion threshold of the cohesive fraction and then on the erosion thresholds for silt fractions. The form of the cohesive-fraction erosion model is similar to the single-class erosion equation of Alishahi and Krone (1964), and is

$$E(gs{=}1) \;=\; M(gs{=}1,bl{=}a)\left[\frac{\tau}{\tau_{ce}(gs{=}1,bl{=}a)} - 1\right]^{n}, \qquad \tau > \tau_{ce}(gs{=}1,bl{=}a) \tag{61}$$

where the cohesive fraction is designated $gs = 1$, the layer bl exposed at the bed surface is designated a, M is an erosion rate constant adjusted for the fraction of cohesive grain-class present in bed layer a, τ is the bed shear stress, and τ_{ce} is the erosion threshold. With the exponent $n = 1$, Equation 61 is similar to the single-grain erosion equations of Kandia (1974) and Ariathurai et al. (1977). If $\tau < \tau_{ce}$ for the cohesive fraction, no sediments are eroded even if the bed shear-stress exceeds the critical threshold for some silts. The critical shear stress for erosion of the cohesive fraction is estimated by a power law depending on the concentration of the cohesive fraction in the bed layer exposed to the flow (Teeter 1987) and generally increases vertically downward in the bed. The erosion rate parameter M is functionally related to the τ_{ce}-value based on Lee and Mehta (1994).

At shear stresses between the upper and lower critical values, a silt sediment fraction will erode or deposit ($0 < P < 1$) at rates linearly related to the bed and threshold shear-stresses, depending on whether or not the cohesive fraction is eroding. Erosion is given precedence in the model such that, for a particular grain class, bed erosion precludes deposition.

The upper or critical erosion threshold shear-stress is defined as the value above which a silt class will remain in suspension. This definition recognizes that erosion of a silt fraction depends first on the condition that the critical shear stress for erosion of the cohesive fraction has been exceeded. Silt fractions must erode in proportion to clay-fraction masses to maintain similarity in the shape of bed and suspended grain-size distributions as discussed in an earlier subsection, and

$$E(gs>1) \ = \ E(gs=1)\frac{S(gs>1,bl=a)}{S(gs=1,bl=a)}\bigg|_{gs>1} \ , \qquad E(gs=1) > 0 \ ; \ \ \tau > \tau_{ce}(gs>1) \quad (62)$$

where $S(gs,bl)$ is the grain-class sediment mass per unit area in a bed layer. Erosion thresholds for silt fractions are taken to be independent of their bed layer location.

Bed-layer model

Erodibility is also linked to the structure of the bed (Dixit 1982), so sediment models often use a layered bed structure (Ariathurai et al. 1977; Teisson 1991; and Hamm et al. 1997). A layered-bed algorithm was developed with variable silt concentrations by layers, depending on initial conditions, and on erosional and depositional history. A fully-settled, near-surface concentration distribution with respect to the cohesive fraction is assumed. After deposition occurs, hindered-settling rate is calculated by bed layer, and material is transported vertically downward in the bed, according to class-aggregated transport parameters, until the specified density distribution is achieved. The sediment mass-conservation equations for bed layer consolidation are

$$\frac{d\,S(gs,bl)}{dt} \ = \ -\frac{W_h(bl)\,S(gs,bl)}{H_s(bl)} \ + \ \frac{W_h(bl-1)\,S(gs,bl-1)}{H_s(bl-1)} \ , \quad H_s(bl) > H_{so}(bl) \quad (63)$$

where $H_s(bl)$ is the bed layer thickness, $H_{so}(bl)$ is the specified fully-settled thickness, and the bed-layer hindered-settling rate is

$$W_h(bl) \ = \ W_{ho}\left[1 \ - \ b_1\sum_{gs=1}^{ns}\frac{S(gs,bl)}{H_s(bl)}\right]^{b_2} \ , \qquad \sum_{gs=1}^{ns}\frac{S(gs,bl)}{H_s(bl)} < \frac{1}{b_1} \quad (64)$$

where ns is the number of grain-size classes, W_{ho} is a reference settling rate, and b_1 and b_2 are grain-class-mass averaged coefficients. Hindered settling is inhibited by deposition or erosion greater than 0.01 g/m²/sec. In the bed, volumes of grain-size classes are taken into account during the conversion between mass and concentration. The sediment mixture is composed of sediment and water. Specifically, it is assumed that

$$H_s(bl) \ = \ \sum_{gs=1}^{ns}\frac{S(gs,bl)}{\rho_s} \ + \ \frac{O_c\,S(gs=1,bl)}{\rho_l} \ + \ \sum_{gs=2}^{ns}\frac{O_s\,S(gs,bl)}{\rho_l} \quad (65)$$

Model Description

where O_c and O_s are the ratios of clay and silt masses to water masses associated with these fractions, and ρ_s and ρ_l are the particle and fluid densities. While mass is transported vertically downward as a result of consolidation, the layer concentration of the cohesive fraction is maintained constant over time, and the condition

$$H_s(bl) = \frac{S(gs=1,bl)}{\rho_s} + \frac{O_c S(gs=1,bl)}{\rho_l} \tag{66}$$

is imposed. Bed layer sediment concentration (mass per unit volume) Cs is $S(gs,bl)/H_s(bl)$.

To reproduce observed hindered settling interface descent curves, some restrictions must be applied due to the discrete nature of the model. The step changes in layer concentration must be such that $(Cs(bl) - Cs(bl-1))/Cs(bl)$ is about constant over depth, and a factor based on this ratio must be applied to W_{ho}. An example of the bed-layer model operation subsequent to a sudden deposition event is shown in Figure 68.

The bed-layer model, based on the kinematic sedimentation theory of Kynch (1952), is a simplification of a number of complex processes. It is intended to be used for calculating the settling and consolidation of thin layers of newly-deposited sediment over time scales of days. For thicker deposits especially, permeability becomes important as the upward velocity of water must equal downward sedimentation (Tan et al. 1990; Pane and Schiffman 1997). At longer times and greater deposit thicknesses, inter-particle stresses develop, and self-weight consolidation occurs. Over an important range of times and concentrations, both sedimentation and self-weight consolidation probably occur (see Toorman and Berlamont 1991).

Bed layers are numbered vertically downward. If a layer is withered away by erosion, it disappears, at least temporarily. The erosion surface thus descends through the bed, as the surface layer thins, then step-wise through progressively deeper layers. The effects of erosion on bed mass are evaluated as

$$\left.\frac{dS(gs,bl=a)}{dt}\right|_e = -E(gs) \tag{67}$$

where a is the exposed bed layer index. Deposition, on the other hand, always occurs into the first layer ($bl = 1$), and the effect of deposition on bed mass is evaluated as

$$\left.\frac{dS(gs,bl=1)}{dt}\right|_d = F(gs) \tag{68}$$

In this way, the bed structure is formed by consolidation from the top layer down. After appreciable deposition has occurred, the bed (in the absence of erosion or further deposition) will eventually return to the specified fully-settled structure.
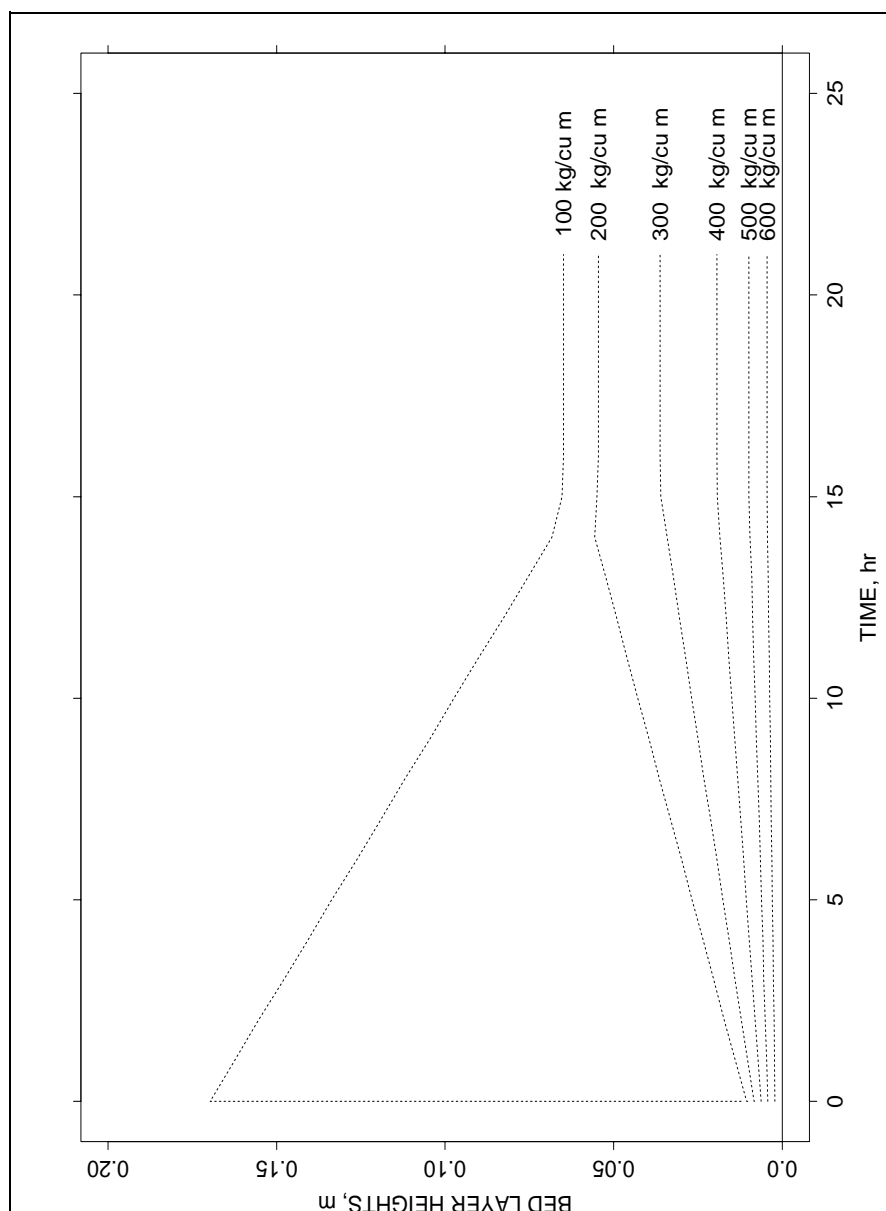
Figure 68. Settling of a 100-kg/m³ bed layer deposited instantaneously just after hour 0.0 showing layer boundaries (also lines of constant concentration) and resulting bed profile

Model Description

As a barrier to excessive winnowing of the cohesive fraction and sorting of grain classes under moderate shear-stress conditions, the model shields a small portion of the cohesive fraction, about equal in magnitude to that proportion deposited with silts, from erosion until coarser grain classes are involved in erosion.

Coefficient adjustment method

The added physical realism of the multiple-grain class formulation allows sediment texture to adjust to hydraulic conditions, but it comes at the price of increased computational burden for operating the model and increased numbers of sediment parameters requiring estimation. Model adjustment was complicated by the somewhat greater numbers of model parameters as compared to a single-grain model formulation. An automated model coefficient adjustment method was developed to expedite model adjustment and to systematize this adjustment so that alternate formulations could be tested objectively.

The adjustment process begins with model coefficients and parameters manually set to rough model-to-prototype TSM agreement. Threshold shear-stress values interpreted from field or experimental data, or typical values found for other systems, are used to start with. Important coefficients were identified, and resuspension model adjustment involved 27 coefficients for the multiple-grain class model. Each model coefficient in this set was varied by a range of factors (typically 0.6 to 1.4) in 10 model simulations, with all other parameters held constant. The variance in the difference between the model results and the field TSM data was used as a criterion of the goodness of the model simulation. If variation of a given coefficient produced a range of variances such that the ratio of the maximum variance to the minimum exceeded a threshold (typically 1.1 to 1.2), then the optimum value of the coefficient was determined for this particular set of other coefficients. After all unknown coefficients were tested in this manner, a new set of model coefficients was developed by applying a weighting to the difference between the original and optimum values and adding those weighted differences to the old coefficient values. Weighting values were 0.33 to 0.5. This procedure was repeated 20 times.

Model tests

Numerical grain-class deposition experiments. The algorithms Equations 57, 59, and 60 were used in a numerical scheme that included mass conservation equations for each grain-size class in a layered sediment bed and a suspension at a point (1-dimension vertical). Model simulations were performed with seven grain-size classes arbitrarily assigned at nominal sizes of 4, 18, 22, 28, 37, 44, and 56 μm. Normally, grain-size classes would be spaced logarithmically by size, but in this case the finest fraction was spaced to accentuate the fine tail of the spectrum. A shear stress was initially imposed (0.16 Pa) greater than τ_{cd} for the clay fraction and less than the τ_{ce} for the next larger class. Numerical deposition experiments were performed by initializing suspensions with grain spectral slopes of $m = 1$, 0, and -1.

Time-series grain-size spectra from the three numerical experiments are shown in Figure 69. The model spectra maintained slopes on their fine ends about the same as initial m's , while the coarse ends deposited. Portions of the clay fraction

of the distribution can be seen in Figure 69 to deposit, even though the imposed shear stress exceeds this class's threshold for deposition.

Numerical steady-state suspension experiments. Mehta and Partheniades (1975) performed annular-flume deposition experiments, starting with high shear stresses. Initially-suspended fine-grained cohesive sediments deposited when shear stresses were reduced, and formed constant, steady-state concentrations that depended on the initial suspension concentrations and the bed shear-stresses. Typical results for one series of experiments are shows in Figure 70. Each experiment had 1 g/l initial concentration of kaolinite. The kaolinite sediment material contained about 35 percent sediment coarser than 2 μm and a maximum particle size of about 45 μm. Similar results were obtained for coarser, fine-grained sediments from San Francisco Bay and Maracaibo Bay, Venezuela. The fractional amount remaining in suspension C_f/C_o for the kaolinite experiments (Mehta and Partheniades 1975) are summarized in Figure 71a. The degree of deposition (1 - C_f/C_o) was found not to depend on initial concentration. This result, plus other experiments on kaolinite suspensions by Partheniades et al. (1968) and Lau and Krishnappan (1994), confirms that these steady-state concentrations were not caused by a balance between erosion and deposition.

The cohesive clay-silt deposition results shown in Figure 70 follow Krone's deposition law for bed shear-stresses less than 0.16 Pa, when all sediment eventually deposited. At higher bed shear stresses, however, they do not follow Krone's deposition law, as only a certain fraction of material, depending on shear-stress, deposited. The times required for deposition to occur and for suspensions to reach steady-state were not greatly affected by the bed shear stress, as can be seen in Figure 70. Material either deposited or remained in suspension, with the transition time consistent with typical settling velocities.

Numerical deposition experiments were performed much the same way as the original experiments. Total suspended material concentrations were initialized at 1 g/l, and shear stresses at 1.05 Pa. A series of 25 model simulations were performed in which shear stresses were reduced to allow deposition.

Plots of example numerical C_f/C_o curves are shown in Figure 71b-c for a single-grain model (ns = 1) and a multiple-grain model (ns = 4), respectively. Multiple-grain classes allow representation of the C_f/C_o curves in a step-wise fashion. The more classes, the better the representation. At times shorter than that required to reach steady-state, multiple-grain class model results have smoother transitions between different shear-stress levels. Model results with ns = 7 after 0.1 and 1 hour for various shear-stress levels are shown in Figures 72a and 72b. These results indicate that, as suspensions approach steady-state values, C/C_o curves take on the stair-step nature as shown in Figure 71b-c, with the finer, slower-settling grain-size classes requiring more time to come to steady-state. The C/C_o curve in Figure 72b can be compared to the observed C_f/C_o curve shown in Figure 71a. Similarly-good results were obtained by a multiple-grain-size class analytic deposition model used to simulate the same experimental data set (Mehta and Lott 1987). In the present model, grain-class coupling is expected to improve the ability to simulate sediment sorting.
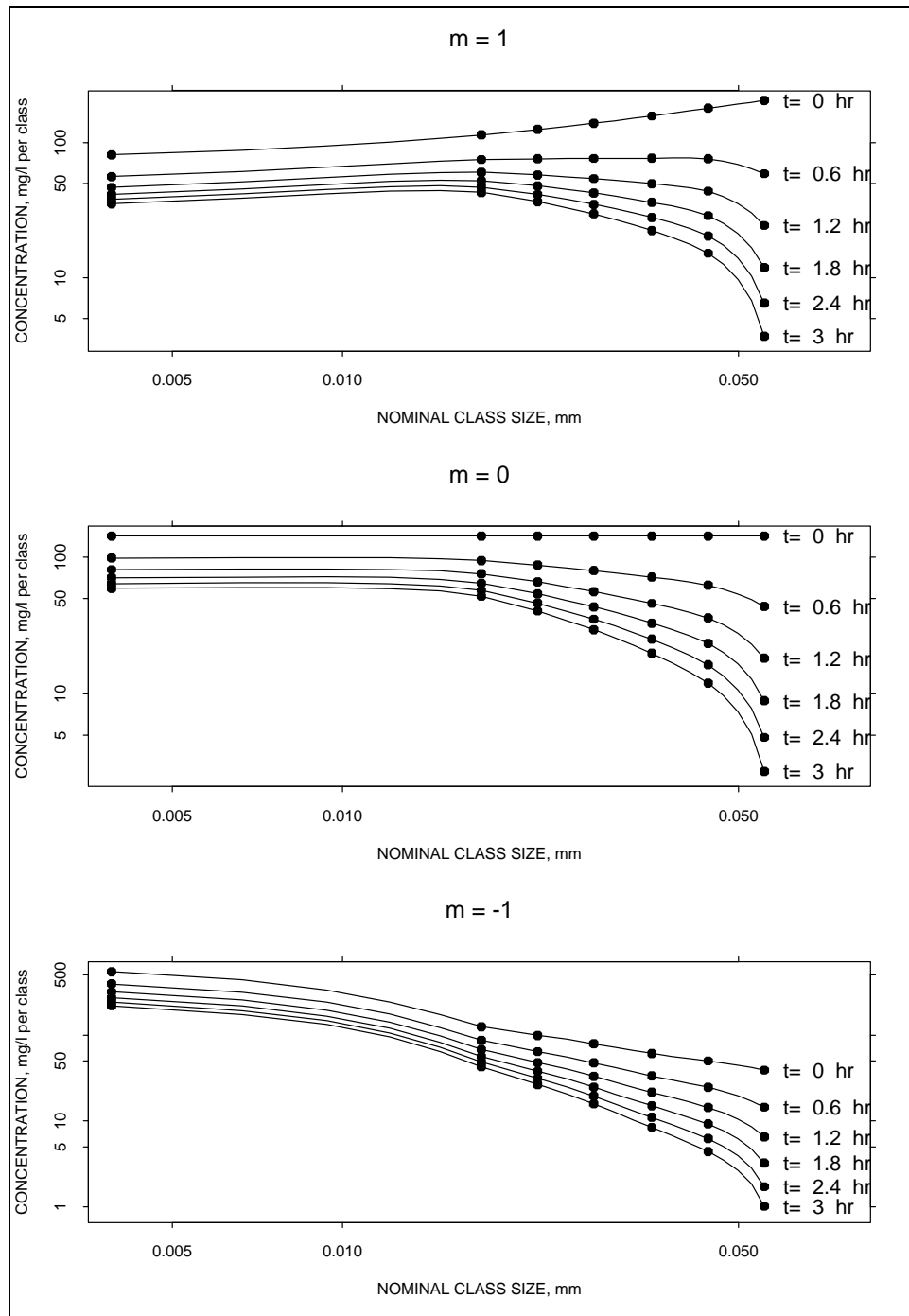
Figure 69. Numerical experiment results for $m = 1$, 0, -1 for deposition under a shear stress of 0.16 Pa
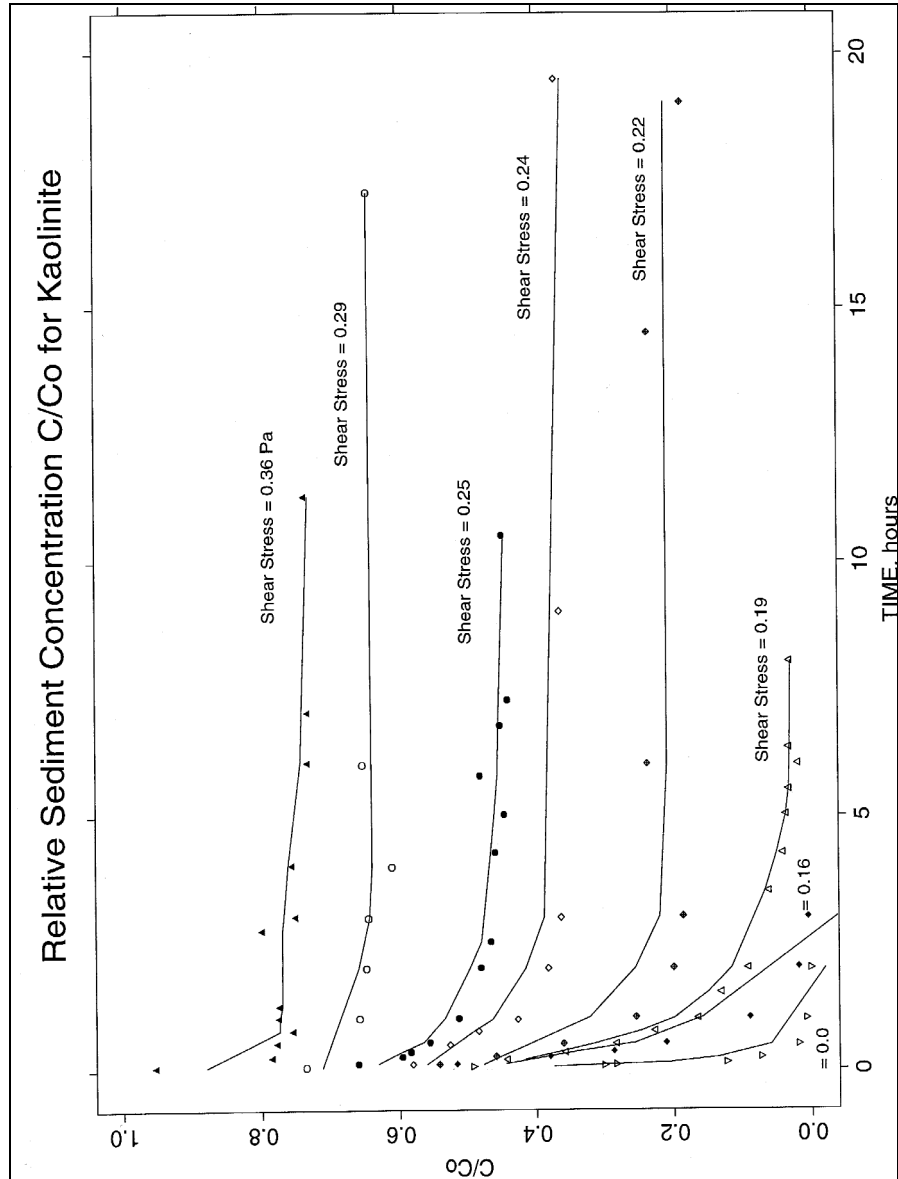
Figure 70. Relative suspension concentration during kaolinite deposition experiments (Mehta and Partheniades 1975). Initial shear stress was 1.05 Pa for all tests
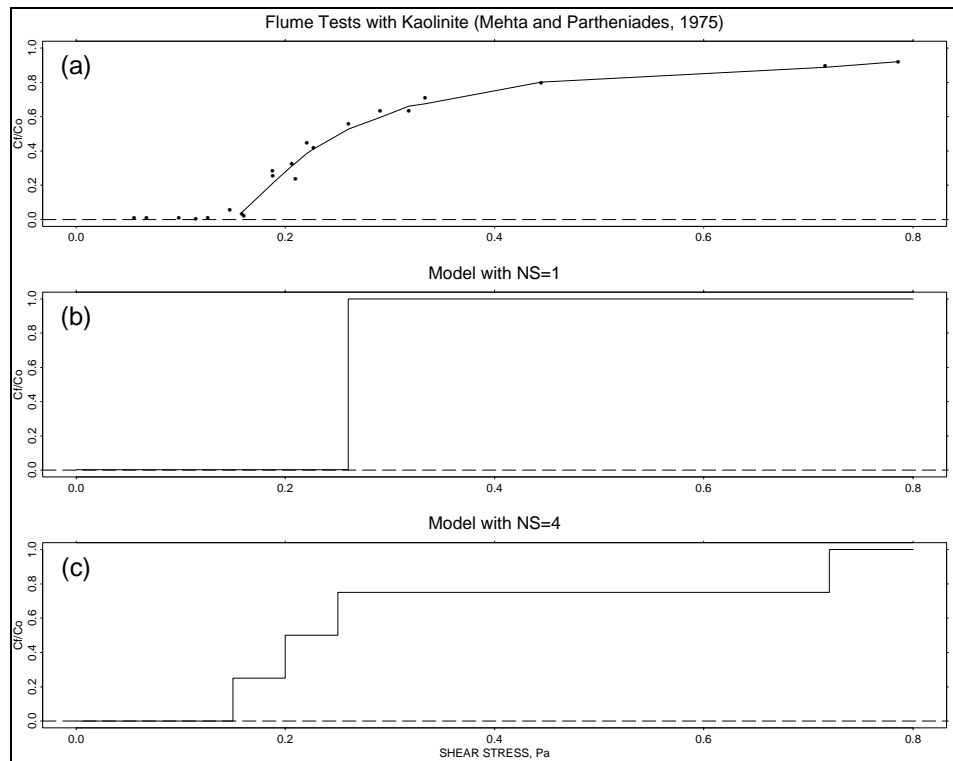
Figure 71. (a) Observed C_f/C_o corresponding to Figure 70, (b) example model result with one grain class, (c) example model result for four grain classes
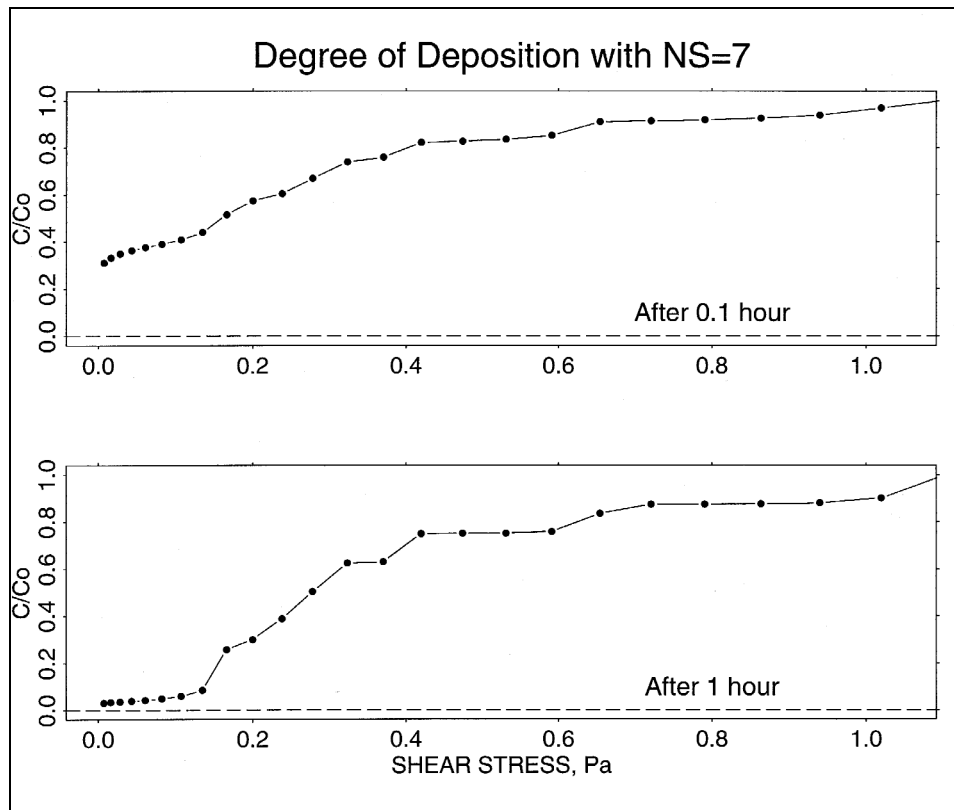
Figure 72. Model relative TSM concentration curves for *ns* = 1 for (a) 0.1 hour, and (b) 1 hour of deposition